Design of two-dimensional half-metals with large spin gaps

Rui-Zi Zhang,[1] Yu-Yang Zhang,[1,*] and Shixuan Du[1,2,†]
[1]*Institute of Physics & University of Chinese Academy of Sciences, Chinese Academy of Sciences, Beijing 100190, People's Republic of China*
[2]*Songshan Lake Materials Laboratory, Dongguan, Guangdong 523808, China*

(Received 5 February 2024; revised 11 June 2024; accepted 30 July 2024; published 13 August 2024)

Two-dimensional (2D) half-metals exhibit promising potential in magnetic nanodevices. However, the discovery of 2D half-metals is still based on a case-by-case evaluation. Here, we propose a general rule to design two-dimensional transition-metal-based half-metals with large spin gaps, namely to find the materials that have a Hund's-rule splitting of the *d* orbitals and a deep anion *p*-orbital energy level that minimizes the *d*-*p* interactions. On the basis of DFT calculations for 54 transition-metal compounds MX_2 ($M = 3d$ block transition metal; $X =$ VIA-VIIA elements) with a distorted tetrahedral crystal field, we found that all the ferromagnetic compounds exhibit half-metallicity. We attribute the half-metallicity to Hund's rule splitting of partially filled *d* orbitals of *M* cations with a weak *d*-*p* orbital hybridization. The chlorides exhibit a spin gap larger than 4 eV, because of the deep Cl *p*-orbital energy level (−8.4 eV). We validate this rule in transition-metal trichlorides $M\mathrm{Cl}_3$ ($M = 3d$ block transition metal). Using this rule, we predict that ferromagnetic monolayer $M\mathrm{Cl}$ and $M_3\mathrm{Cl}_8$ ($M = 3d$ block transition metal) are half-metals with large band gaps. This work enriches the variety of 2D half-metals and could lead to novel magnetic nanodevices.

DOI: 10.1103/PhysRevB.110.085130

I. INTRODUCTION

Two-dimensional (2D) materials with intrinsic magnetism have attracted considerable interest for potential applications in nanodevices [1–5]. Among the newly emerged 2D magnets, half-metals would be especially suitable for magnetic-storage devices since one spin channel is metallic while the other is insulating, i.e., they feature 100% spin polarization. A 100% spin polarization will lead to an ultrahigh tunnelling magnetoresistive (TMR) ratio and largely increase the areal density of magnetic-storage devices [6]. Since the prediction of the first half-metallic material, NiMnSb [7], a number of half-metallic bulk compounds have been identified, such as transition-metal oxides [8,9], perovskites [10,11], zinc-blende compounds [12,13], and Heusler alloys [14,15]. In recent years, half-metallicity has been predicted in many 2D materials, such as transition-metal dihalides $\mathrm{Fe}X_2$ ($X =$ Cl, Br, I) [16,17], transition-metal compounds $\mathrm{Mn}X$ ($X =$ P, As) [18], and transition-metal trichlorides [19–22]. Moreover, some semiconducting materials, such as PdSe_2 [23], CrI_3 [24], and CrCl_3 [25], also exhibit half-metallicity when doped.

The spin gap, which is defined as the band gap of the insulating spin channel, is a parameter that affects the device performance of 2D half-metals [26,27]. The temperature fluctuations or carrier doping in the devices degrade the half-metallicity while large spin gaps resist the influence of temperature fluctuations or carrier doping and maintain the half-metallicity for devices [28–30]. The known 2D half-metals feature spin gaps ranging 0.3–6.0 eV [27,31–36]. The spin gap is affected by many factors, such as crystal structure, the component elements, doping conditions, and so on. The available literature suggests that the discovery of half-metals and the determination of the spin gap are based on a case-by-case evaluation. However, the known 2D half-metals are compounds of transition-metal and group-VA-VIIA elements with different crystal structures. The similar components indicate that the form of half-metallicity may follow some broader rules. A general rule would be useful to describe how the crystal structure and the components affect the spin gap and potentially guide the design of 2D half-metals.

In this paper, we propose a general rule to design two-dimensional transition-metal-based half-metals (half-metallic ferromagnets) with large spin gaps. We first discuss the half-metallicity in 2D transition-metal compounds MX_2 with distorted tetrahedral crystal field ($M = 3d$ block transition-metal element; $X =$ VIA-VIIA elements). On the basis of DFT calculations for MX_2, all the ferromagnetic compounds are half-metals, while the chlorides exhibit the largest spin gaps (>4 eV). The cation *d* orbitals tend to split according to Hund's rule and induce half-metallicity when the *d* orbitals are partially occupied. Thus, we propose a *d*-*p* half-metallicity rule: the combination of cations with Hund's-rule splitting of *d* orbitals and anions with a deep *p*-orbital energy level leads to a half-metal with a large spin gap with weak *d*-*p* orbital hybridization. We validate this rule in transition-metal trichlorides $M\mathrm{Cl}_3$ ($M = 3d$ block transition metal). Using this rule, we tune the number of *d* electrons of cations by adjusting the number of anions and predict that ferromagnetic monolayer $M\mathrm{Cl}$ and $M_3\mathrm{Cl}_8$ ($M = 3d$ block transition metal)

*Contact author: zhangyuyang@ucas.ac.cn
†Contact author: sxdu@iphy.ac.cn

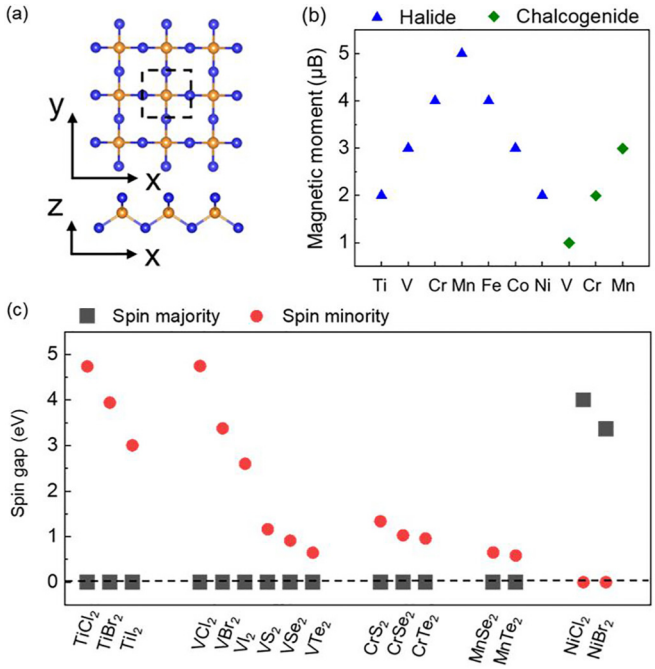

FIG. 1. Crystal structure and half-metallicity of monolayer MX_2 (M = Sc, Ti, V, Cr, Mn, Fe, Co, Ni, Cu; X = S, Se, Te, Cl, Br, I) with distorted tetrahedral crystal field. (a) Top view and side view of the structures of MX_2. Here, orange and blue balls indicate transition-metal and chalcogen/halogen elements, respectively. The dashed line indicates the unit cell. (b) Magnetic moments of MX_2. The blue triangles and the olive rhombi indicate the chalcogenides and halides, respectively. (c) Spin gaps of MX_2. All the ferromagnetic ground state materials are listed here. The red circles and the black squares indicate that the gaps are from majority-spin channel and minority-spin channel, respectively.

are half-metals with large band gaps. These results provide guidance for the discovery of half-metals with large spin gaps.

II. RESULTS

We first discuss the half-metallicity in 2D transition-metal compounds MX_2 with distorted tetrahedral crystal field. We combine all transition-metal elements in the 3d row of the periodic table with elements in the VIA-VIIA groups (M = 3d transition-metal element; X = VIA-VIIA element). Figure 1(a) shows the top view and side view of the MX_2 atomic structures with a D_{2d} symmetry. Each M cation is connected with four X anions, constituting a distorted tetrahedron. The X anions form distorted tetrahedral cages and the centered M cations form a square lattice [37]. The distorted tetrahedral cages change the symmetry and have an influence on orbitals splitting under crystal field. The stability of these materials is checked by phonon calculations. The phonon dispersions of partial structural stable MX_2 are shown in Fig. S1 of the Supplemental Material (SM) [38].

Among the stable MX_2, we identify the magnetic ground states via density functional theory (DFT) calculations by comparing the energies between ferromagnetic (FM), D-type antiferromagnetic (D-AFM), G-type antiferromagnetic (G-AFM), and nonmagnetic (NM) ordering, as shown in Figs. S2a–S2c. The magnetic ground states of these materials are shown in Fig. S2d. All the structural stable dihalides, except NiI_2, exhibit magnetic ground states. The MX_2 (M = Ti, V, Ni) exhibit a ferromagnetic ground state while those with M = Mn, Fe, Co have a G-AFM ground state. Among the magnetic dichalcogenides, the MX_2 exhibits FM ground states for M = V, Cr, Mn. We further analyze the thermal stability of MX_2 among the dynamical stable compounds via the energy above hull ($E_{\rm hull}$). The $E_{\rm hull}$ of the MCl_2 is less than 100 meV/atom except for $TiCl_2$, which suggests a large possibility to be synthesized (as shown in Table S1 of the Supplemental Material [38]). As shown in Table S2, the exfoliation energy ($E_{\rm ex}$) of most MCl_2 compounds is comparable with that of graphene and layered TMD materials [39]. We also calculated the Curie temperature (T_C) which is shown in Table S3 (see the Supplemental Material (SM) [38]).

The magnetic moments of ferromagnetic MX_2 compounds are shown in Fig. 1(b). The magnetic moments of halides correspond to the number of d electrons up to 5 μ_B for MnX_2 and decrease with further increase of the number of d electrons. It is clear that the net magnetic moment is proportional to the number of unpaired d electrons of cations. The chalcogenides behave in a similar way, but their number is limited to just three compounds.

We employed DFT calculations and further found that all of the ferromagnetic MX_2 compounds are half-metals with various spin gaps. The half-metallicity and spin gap of MX_2 compounds are shown in Fig. 1(c). DFT calculations show that the spin gaps of halides are larger than 2.5 eV (larger than 4 eV for chlorides), while the spin gaps of chalcogenides are ~1 eV. In addition, the spin gaps decrease roughly linearly from chlorides to iodides. This feature can be explained by the trend in the halogen p-orbital energy level. The large spin gap of chlorides results from the deep Cl p-orbital energy level (−8.4 eV). This level gets shallower for the higher-Z halogen, but it is still fairly deep at −7.1 eV for I, while the Te p energy level is at −5.9 eV. Thus, transition-metal chlorides are the half-metals with the largest spin gaps.

III. DISCUSSION

We now use $TiCl_2$ and $NiCl_2$ as examples to explore the half-metallicity of MX_2 compounds. Figures 2(a) and 2(b) show the projected density of states (PDOS) of M-atom d orbitals and X-atom p orbitals of monolayer $TiCl_2$ and $NiCl_2$ with ferromagnetic ground state, which presents the cases of $d < 5$ and $d > 5$, respectively. The orange and blue curves indicate the PDOS of the d orbitals of the M cations and p orbitals of the X anions, respectively. The d orbitals are located within the gap of occupied p orbitals of anions and empty orbitals. The two spin channels exhibit metallic and insulating behavior, respectively. Such PDOS results in the half-metallicity for $TiCl_2$ and $NiCl_2$. The insulating spin channel stems from the minority-spin channel for $TiCl_2$ and from the majority-spin channel for $NiCl_2$. Figures S3a and S3b further show the band structure of monolayer $TiCl_2$ and $NiCl_2$. Based on the band structure, the spin gap of $TiCl_2$ and $NiCl_2$ are direct and occur at the G point, ranging 4.0–4.9 at the PBE level (see the Supplemental Material (SM) [38]).

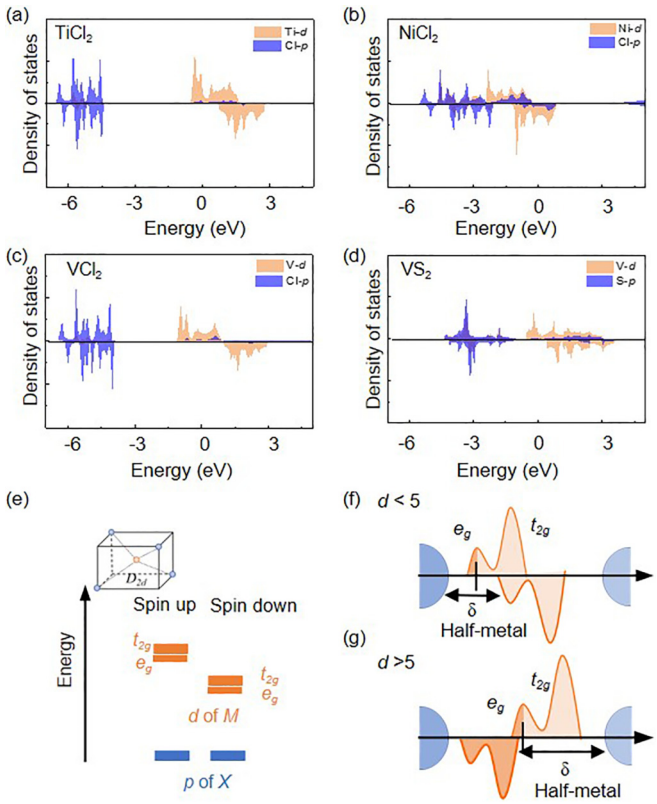

FIG. 2. The mechanism of the half-metallicity of 2D MX_2. (a)–(d) The spin-polarized PDOS on the M-atom d orbitals and the X-atom p orbitals of some half-metallic compounds of 2D MX_2. (e) The distribution of d orbitals based on crystal field theory. (f),(g) Schematic of the d-orbital splitting of 2D MX_2 compounds for fewer than five and more than five d electrons of M cations, respectively. The black horizontal lines indicate the Fermi energy and δ indicates the spin gap.

To further explore the relation between the size of the spin gap and the choice of anion elements, we further calculate the PDOS of VCl_2 and VS_2, which is shown in Figs. 2(c) and 2(d). It is found that the spin gaps of VCl_2 and VS_2 are 4.5 and 1.0 eV, respectively. Similar with $TiCl_2$ and $NiCl_2$, the spin gaps are direct and occur at the G point (Figs. S3c and S3d). The large difference in the spin gap between these two materials is mainly attributed to the positions of the p orbitals of X anions, which are at -4.0 and -1.0 eV for VCl_2 and VS_2, respectively. The difference in the spin gap mainly results from the depth of the anion energy levels, which indicates that the spin gap is mainly affected by the depth of the anion p energy level.

To understand the mechanism of the half-metallicity of the ferromagnetic MX_2 compounds, we build a model to describe the electron distribution based on d-p interactions. In the distorted tetrahedral crystal field, the t_{2g} and e_g states merge together and induce the vanishing of the energy gap in between, as shown in Fig. 2(e). Meanwhile, the d electrons of M cations tend to occupy one spin channel due to the large spin-pairing energy of $3d$ orbitals and the small orbital splitting energy induced by the merging of t_{2g} and e_g states. As a result, the energy of d orbitals in the majority-spin channel is lower than that of the d orbitals in the majority-spin channel. Hence, the d orbitals of M cations exhibit Hund's-rule splitting and induce half-metallicity in different electron occupations. The d orbitals of M cations split into t_{2g} and e_g states with an energy gap in an ideal tetrahedral crystal field. In this case, the half-metal could turn to semiconductor when one of the t_{2g} or e_g states is fully filled and the other is empty.

Following up with Hund's rule splitting, the majority spin channel is partially occupied while the minority spin channel is empty when the number of d electrons is smaller than 5. In this case, a half-metallic state is formed, and the spin gap δ is defined between the lowest empty d band of the minority spin channel and p orbitals of anions, as shown in Fig. 2(f). When the number of d electrons is larger than 5, the material is a half-metal and the spin gap δ is defined between the highest occupied d band of the majority spin channel and the empty orbitals, as shown in Fig. 2(g). Moreover, when there are five d electrons, the majority spin channel is fully occupied and the material becomes a semiconductor or semimetal instead of a half-metal. Therefore, a ferromagnetic system is half-metallic if the number of d electrons is not 5. The relation between the magnetic moment and the number of d electrons of M cations also originated from this Hund's-rule splitting of d orbitals.

As shown above, the spin gap δ in the d-p coupling system is defined between unfilled/fully filled d orbitals of cations and p orbitals of the anions/empty states. Here, the d orbitals are around the Fermi level and the depth of the p orbitals of X anions affect the size of the spin gap. Hence, the form of half-metal in a d-p coupled system is determined by the d electrons of cations, while the size of the spin gap is mainly affected by the p orbitals of the anions. We name this rule "d-p half-metallicity rule." According to this d-p half-metallicity rule, a half-metal with a large spin gap is obtained by selecting cations with the Hund's-rule splitting of d orbitals and anions with deep p-orbital energy levels. The Hund's-rule splitting of d orbitals in the rules stems from the weak d-p orbital hybridization.

The proposed rule is general regarding the types of crystal fields, that yield the splitting of d orbital. Taking the octahedral crystal field as an example, the distribution of d orbitals of the octahedral crystal field with weak d-p orbital hybridization are shown in Fig. 3(a). Different from the distorted tetrahedral crystal field, one gap locates between t_{2g} and e_g states in one spin channel. This indicates there should be a semiconductor instead of a half-metal when the t_{2g} states are fully filled while the e_g states are empty. For example, the half-metals turn to semiconductors when the number of d electrons increases to 3 from 2, as shown in Figs. 3(b) and 3(c). The occurrence of semiconductors is due to the specific crystal structure and is in the scope of the d-p half-metallicity rule.

To validate the proposed rule, we explore the half-metallicity in MCl_3. The crystal structure of monolayer MCl_3 is shown in Fig. 3(d). The transition-metal cation is surrounded by six anions (octahedral crystal field). We calculated the PDOS of VCl_3 and $CrCl_3$ in which the number of d electrons of V^{3+} and Cr^{3+} cations are 2 and 3, respectively. For monolayer VCl_3 [Fig. 3(e)], d orbitals split into t_{2g} and e_g groups and exhibit half-metallicity due to the partially filled t_{2g} orbitals of the majority-spin channel. For monolayer $CrCl_3$ [Fig. 3(f)], the PDOS reveals that in the majority-spin channel

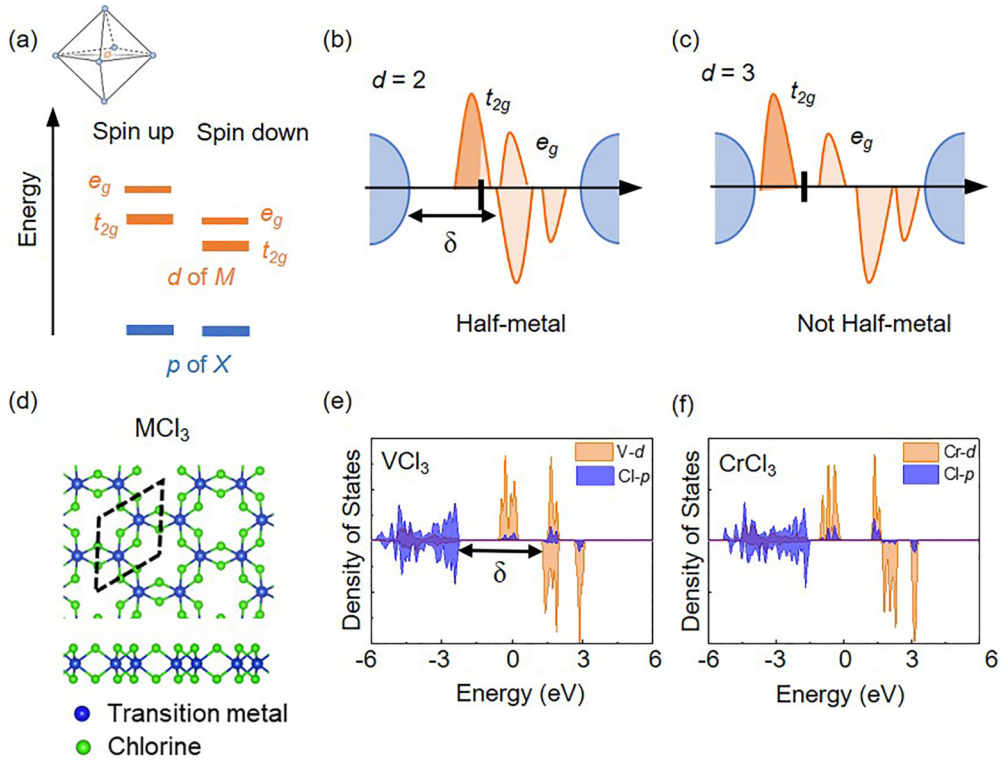

FIG. 3. The half-metallicity of 2D MCl_3 with octahedral crystal field. (a) The distribution of d orbitals of octahedral crystal field. (b),(c) The schematic of the d orbital splitting for different d electrons of M cations. (d) Top view and side view of the structures of 2D MCl_3. (e),(f) The spin polarized PDOS of 2D VCl_3 and $CrCl_3$.

of $CrCl_3$, the t_{2g} orbitals are fully filled and the e_g orbitals are empty, which induces a t_{2g}-e_g gap in the majority-spin channel. This t_{2g}-e_g gap in the majority-spin channel turns the would-be metallic spin channel to insulating, resulting in a half-metal to semiconductor transition in monolayer $CrCl_3$.

Based on the proposed rule, monolayer $TiCl_3$, VCl_3, $MnCl_3$, $CoCl_3$, and $NiCl_3$ are half-metal. For monolayer $FeCl_3$ and $CuCl_3$, the number of d electrons of cations is 5 and 8, respectively, resulting in the semiconducting behavior. While for monolayer $CuCl_3$ ($d = 8$), similar to the $CrCl_3$ ($d = 3$) condition, the existence of a t_{2g}-e_g gap in the minority spin channel also makes this material semiconducting. The results of the DFT calculation verify our prediction, as shown in Fig. S4. Previous works have also found that monolayer VCl_3, $MnCl_3$, and $NiCl_3$ are half-metals [19–21] while monolayer $CrCl_3$ and $FeCl_3$ are semiconductors [40–42]. It is worth noting that when X atoms just above and just below the central layer relax and change distance from the central layer with a small distance, the electronic structures are qualitatively the same (see more discussion in Fig. S5).

We then use the proposed rule to predict new half-metals with large spin gaps. Based on the rule, 2D transition-metal chlorides are the best candidates to form half-metals with large spin gaps due to the weak d-p orbital hybridization and deep p-orbital energy levels. Meanwhile, the d electrons of the cation determine the form of half-metal. This indicates we can predict the half-metal by changing the number of d electrons of cations. For example, monolayer $FeCl_3$ (number of d electrons of cations = 5) we mentioned above are semiconductors while $FeCl_2$ [15] (number of d electrons of cations = 6) are proven to be half-metals. Furthermore, the half-metallicity should be maintained when the number of d electrons of cations = 7, i.e., FeCl. Here, we adopt monolayer FeCl crystal structure as shown in Fig. 4(a). Based on our rule, the 7 d electrons of the Fe cation will lead to fully occupied majority-spin channel and partially occupied minority-spin channel and induce a spin gap in the majority-spin channel, as shown in Fig. 4(b). To verify the prediction, we plot the PDOS of FeCl [Fig. 4(c)] and find the consistency with our prediction.

Comparing with the integral d electrons of cations, the fractional also induces half-metallicity in our rules. We can tune the number of d electrons of cations by changing the number of Cl anions. For example, monolayer $MnCl_3$ is half-metal due to the number of d electrons of cations being 4. Mn_3Cl_8 creates one Cl vacancy for each three-unit cell and adopt a similar crystal structure with $MnCl_3$, as shown in Fig. 4(b). Based on our rule, ferromagnetic Mn_3Cl_8 should be half-metal with partially occupied majority-spin channel and empty minority-spin channel and induce spin gap in minority-spin channel, as shown in Fig. 4(e). We calculate the PDOS of Mn_3Cl_8 and find the half-metallicity, as shown in Fig. 4(f).

We further find more half-metals based on the crystal structure of FeCl and Mn_3Cl_8. According to previous research, CoCl is the only stable magnetic compound except FeCl [43] while V_3Cl_8 [44] and Nb_3Cl_8 [45] are proven to be stable. We calculate the PDOS of ferromagnetic FeCl, V_3Cl_8, and Nb_3Cl_8, and find the half-metallicity which is consistent with

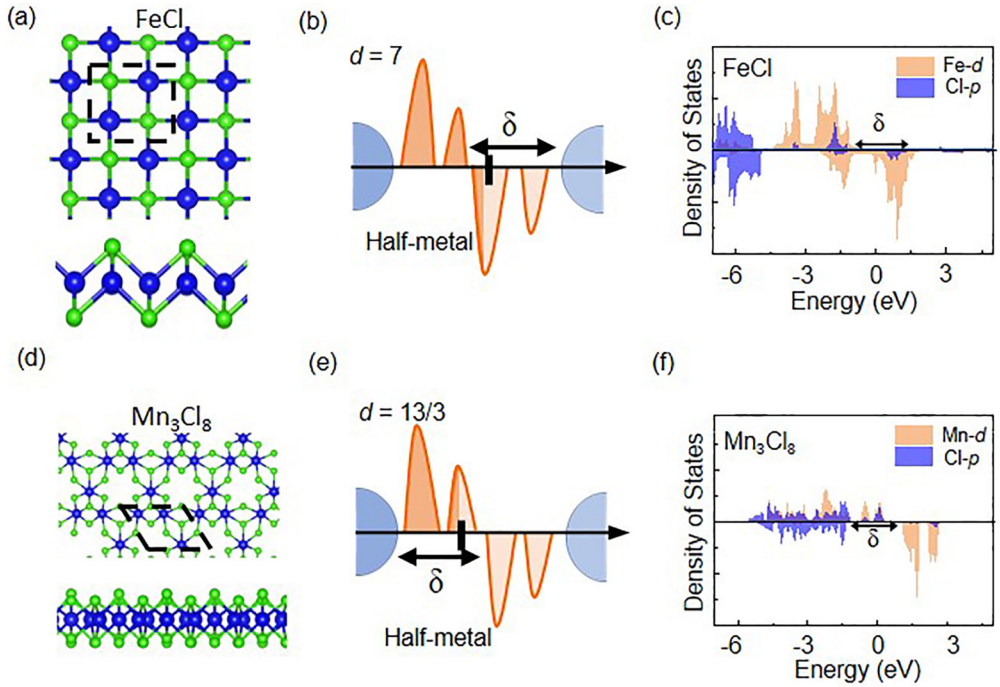

FIG. 4. The prediction of half-metallicity of 2D transition-metal chlorides. Top view and side view of the structures of 2D materials FeCl (a) and Mn_3Cl_8 (d). (b),(c) The schematic of the *d* orbital splitting and corresponding PDOS of FeCl. (e),(f) The schematic of the *d* orbital splitting and corresponding PDOS of Mn_3Cl_8.

the proposed rule, as shown in Fig. S6. The half-metals with fractional *d* electrons indicate we can design more half-metals by adjusting the number of anions or anion elements.

The rule can be applied to more 2D materials in addition to 2D materials with *d*-*p* hybridization. According to Ref. [46], the lanthanide-based *MX*enes also exhibit half-metallicity. The half-metallicity is attributed to the Hund's-rule splitting of the *f* orbitals of lanthanide elements. The compound Gd_2CF_2 is a semiconductor, which results from the two insulating spin channels, i.e., fully occupied majority-spin channel and empty minority-spin channel. Compared with bulk materials, the Hund's-rule splitting of transition-metal elements is more common in 2D materials. This feature can be attributed to the smaller influence of direct interactions of transition-metal elements in 2D materials.

It is worth noting that the *d*-*p* half-metallicity rule is valid only for a weak *d*-*p* hybridization since the rule is based on the crystal field theory. Usually, the stronger electronegativity of *X* element (halogen) and lower number of *M*-*X* bond can lead to weak hybridization. For strong *d*-*p* hybridization condition, such as $CrSe_2$, the strong *d*-*p* hybridization diminishes the bonding-antibonding gap, and induces the merging of *p* and *d* orbitals, resulting in a metallic behavior (as shown in Fig. S7). To quantitatively estimate the hybridization, we define strength of hybridization (SOH) as the ratio of the hybridized *d* orbital to the total *d* orbital. The SOH of the half-metal we mentioned is up to 0.26 while the SOH of $CrSe_2$ is 0.35 (as shown in Table S4). The strong *d*-*p* interaction also enhances the superexchange interaction via Cr-Se-Cr, and induces the partially filled *d* orbitals in a minority-spin channel around the Fermi level, which also contributes to the metallicity in monolayer $CrSe_2$.

IV. CONCLUSIONS

In conclusion, we propose a *d*-*p* half-metallicity rule to find the 2D half-metals with large spin gap based on the *d*-*p* orbital interaction, which amounts to selecting cations with Hund's-rule splitting of *d* orbitals and anions with deep *p* orbital energy level. We predict that the ferromagnetic transition-metal compounds MX_2 (M = Ti, V, Cr, Mn, Fe, Co, Ni; X = Cl, Br, I, S, Se, Te) are all half-metals when the *d* electrons are not 5 for each cation. Meanwhile, the halides exhibit the largest spin gaps. We then validate the *d*-*p* half-metallicity rule in ferromagnetic transition-metal compounds MCl_3 (M = Ti, V, Cr, Mn, Fe, Co, Ni, Cu) which can be regarded as prototype systems containing octahedral crystal field. By applying the rule, we find some different half-metals FeCl and Mn_3Cl_8 and apply the rule to the 2D materials with *f*-*p* orbital interaction. The *d*-*p* half-metallicity rule provides a different perspective to guide the design of the half-metals with large spin gaps.

V. COMPUTATIONAL METHODS

The calculations were performed using the Vienna *ab initio* simulation package (VASP) [47,48]. The projector augmented wave (PAW) method [49] was applied. A plane wave basis set with a cutoff energy of 700 eV was used to expand the wave functions. For the exchange and correlation, we mainly employed the Perdew-Burke-Ernzerhof (PBE) functionals [50]. Atomic coordinates were fully optimized until the forces were smaller than 0.01 eV/Å. We used a vacuum spacing of 20 Å, which reduced the image interactions caused by the periodic boundary conditions. Phonon spectra were calculated with the finite displacement method and the PBE functional using the PHONOPY code [51] and a supercell was

up to 5 × 5. Brillouin-zone integration was carried out using 24 × 24 × 1 Monkhorst-Pack k-point meshes for all the calculated materials. The structure figures were produced with VESTA.

We checked the ground states of 2D materials by employing both the HSE06 functional [52] and PBE functional. It is found that except for $CoCl_3$ and $CrSe_2$, PBE and HSE06 give the same magnetic order. While applying Dudarev's approach with a $U = 1.5$ and 4 eV for $CoCl_3$ and $CrSe_2$, the PBE + U gave the same magnetic order for $CoCl_3$ and $CrSe_2$ as the HSE06 functional. It is widely believed that PBE functional underestimated the energy gaps but did not change the order of d orbitals of M cations [53–55]. Considering that it is the d orbitals of M cations but not the energy order that plays the important role in our analysis, to save calculation resources, we used the PBE functional in the DOS calculation (PBE + U for $CoCl_3$ and $CrSe_2$). To check the difference between PBE and HSE06 in our analysis, we plotted the DOS of $NiCl_2$ in Fig. S8 [see the Supplemental Material (SM) [38]]. It is confirmed that PBE and HSE06 gave the same conclusion. We also plotted the DOS with PBE + U functional to check the half-metallicity; the results (Fig. S9) show that the PBE + U did not change the half-metallicity [see the Supplemental Material (SM) [38]].

ACKNOWLEDGMENTS

We thank Prof. S. T. Pantelides at Vanderbilt University for the constructive suggestions and discussions. This work was supported by the National Natural Science Foundation of China (Grants No. 52250402 and No. 61888102), the National Key R&D Program of China (Grants No. 2019YFA0308500 and No. 2022YFA1204100), CAS Project for Young Scientists in Basic Research (Grant No. YSBR-003), and the Fundamental Research Funds for the Central Universities. A portion of the research was performed in CAS Key Laboratory of Vacuum Physics.

[1] C. Gong and X. Zhang, Two-dimensional magnetic crystals and emergent heterostructure devices, Science **363**, 706 (2019).

[2] Z. Wang, T. Zhang, M. Ding, B. Dong, Y. Li, M. Chen, X. Li, J. Huang, H. Wang, X. Zhao *et al.*, Electric-field control of magnetism in a few-layered van der Waals ferromagnetic semiconductor, Nat. Nanotechnol. **13**, 554 (2018).

[3] Z. Wang, D. Sapkota, T. Taniguchi, K. Watanabe, D. Mandrus, and A. F. Morpurgo, Tunneling spin valves based on Fe_3GeTe_2/hBN/Fe_3GeTe_2 van der Waals heterostructures, Nano Lett. **18**, 4303 (2018).

[4] I. A. Verzhbitskiy, H. Kurebayashi, H. Cheng, J. Zhou, S. Khan, Y. P. Feng, and G. Eda, Controlling the magnetic anisotropy in $Cr_2Ge_2Te_6$ by electrostatic gating, Nat. Electron. **3**, 460 (2020).

[5] S. Manipatruni, D. E. Nikonov, C.-C. Lin, T. A. Gosavi, H. Liu, B. Prasad, Y.-L. Huang, E. Bonturim, R. Ramesh, and I. A. Young, Scalable energy-efficient magnetoelectric spin–orbit logic, Nature (London) **565**, 35 (2019).

[6] B. Dieny, I. L. Prejbeanu, K. Garello, P. Gambardella, P. Freitas, R. Lehndorff, W. Raberg, U. Ebels, S. O. Demokritov, J. Akerman *et al.*, Opportunities and challenges for spintronics in the microelectronics industry, Nat. Electron. **3**, 446 (2020).

[7] R. A. de Groot, F. M. Mueller, P. G. van Engen, and K. H. J. Buschow, New class of materials: Half-metallic ferromagnets, Phys. Rev. Lett. **50**, 2024 (1983).

[8] K. Schwarz, CrO_2: Predicted as a half-metallic ferromagnet, J. Phys. F **16**, L211 (1986).

[9] Z. Zhang and S. Satpathy, Electron states, magnetism, and the Verwey transition in magnetite, Phys. Rev. B **44**, 13319 (1991).

[10] K. I. Kobayashi, T. Kimura, H. Sawada, K. Terakura, and Y. Tokura, Room-temperature magnetoresistance in an oxide material with an ordered double-perovskite structure, Nature (London) **395**, 677 (1998).

[11] Y. P. Liu, S. H. Chen, H. R. Fuh, and Y. K. Wang, First-principle calculations of half-metallic double perovskite $La_2BB'O_6$ (B,B'=3d transition metal), Commun. Comput. Phys. **14**, 174 (2013).

[12] H. Akinaga, T. Manago, and M. Shirai, Material design of half-metallic zinc-blende CrAs and the synthesis by molecular-beam epitaxy, Jpn. J. Appl. Phys. **39**, L1118 (2000).

[13] B.-G. Liu, Robust half-metallic ferromagnetism in zinc-blende CrSb, Phys. Rev. B **67**, 172411 (2003).

[14] S. Skaftouros, K. Özdoğan, E. Şaşıoğlu, and I. Galanakis, Generalized Slater-Pauling rule for the inverse Heusler compounds, Phys. Rev. B **87**, 024420 (2013).

[15] K. Özdoğan, E. Şaşıoğlu, and I. Galanakis, Slater-Pauling behavior in LiMgPdSn-Type multifunctional quaternary Heusler materials: Half-metallicity, spin-gapless and magnetic semiconductors, J. Appl. Phys. **113**, 193903 (2013).

[16] M. Ashton, D. Gluhovic, S. B. Sinnott, J. Guo, D. A. Stewart, and R. G. Hennig, Two-dimensional intrinsic half-metals with large spin gaps, Nano Lett. **17**, 5251 (2017).

[17] E. Torun, H. Sahin, S. K. Singh, and F. M. Peeters, Stable half-metallic monolayers of $FeCl_2$, Appl. Phys. Lett. **106**, 192404 (2015).

[18] B. Wang, Y. Zhang, L. Ma, Q. Wu, Y. Guo, X. Zhang, and J. Wang, MnX (X = P, As) monolayers: A new type of two-dimensional intrinsic room temperature ferromagnetic half-metallic material with large magnetic anisotropy, Nanoscale **11**, 4204 (2019).

[19] J. He, S. Ma, P. Lyu, and P. Nachtigall, Unusual Dirac half-metallicity with intrinsic ferromagnetism in vanadium trihalide monolayers, J. Mater. Chem. C **4**, 2518 (2016).

[20] Q. Sun and N. Kioussis, Prediction of manganese trihalides as two-dimensional Dirac half-metals, Phys. Rev. B **97**, 094408 (2018).

[21] Z. Li, B. Zhou, and C. Luan, Strain-tunable magnetic anisotropy in two-dimensional Dirac half-metals: Nickel trihalides, RSC Adv. **9**, 35614 (2019).

[22] J.-Y. You, C. Chen, Z. Zhang, X.-L. Sheng, S. A. Yang, and G. Su, Two-dimensional Weyl half-semimetal and tunable quantum anomalous Hall effect, Phys. Rev. B **100**, 064408 (2019).

[23] S.-H. Zhang and B.-G. Liu, Hole-doping-induced half-metallic ferromagnetism in a highly-air-stable $PdSe_2$ monolayer under uniaxial stress, J. Mater. Chem. C **6**, 6792 (2018).

[24] Y. Zhao, J.-J. Zhang, S. Yuan, and Z. Chen, Nonvolatile electrical control and heterointerface-induced half-metallicity of 2D ferromagnets, Adv. Funct. Mater. **29**, 1901420 (2019).

[25] Y. Gao, J. Wang, Y. Li, M. Xia, Z. Li, and F. Gao, Point-defect-induced half metal in $CrCl_3$ monolayer, Phys. Status Solidi Rapid Res. Lett. **12**, 1800105 (2018).

[26] G. Bhattacharyya, I. Choudhuri, P. Bhauriyal, P. Garg, and B. Pathak, Ferromagnetism in magnesium chloride monolayer with an unusually large spin-up gap, Nanoscale **10**, 22280 (2018).

[27] J.-Y. Chen, X.-X. Li, W.-Z. Zhou, J.-L. Yang, F.-P. Ouyang, and X. Xiong, Large-spin-gap nodal-line half-metal and high-temperature ferromagnetic semiconductor in Cr_2X_3 (X = O, S, Se) monolayers, Adv. Electron. Mater. **6**, 1900490 (2020).

[28] M. Jourdan, J. Minár, J. Braun, A. Kronenberg, S. Chadov, B. Balke, A. Gloskovskii, M. Kolbe, H. J. Elmers, G. Schönhense *et al.*, Direct observation of half-metallicity in the Heusler compound Co_2MnSi, Nat. Commun. **5**, 3974 (2014).

[29] G. Jana, A. Joshi, S. Pal, and A. Mukherjee, Emergent half-metal at finite temperatures in a Mott insulator, Commun. Phys. **5**, 66 (2022).

[30] X. Li, X. Wu, and J. Yang, Half-metallicity in $MnPSe_3$ exfoliated nanosheet with carrier doping, J. Am. Chem. Soc. **136**, 11065 (2014).

[31] Q. Ma, W. Wan, Y. Li, and Y. Liu, First principles study of 2d half-metallic ferromagnetism in Janus Mn_2XSb (X = As, P) monolayers, Appl. Phys. Lett. **120**, 112402 (2022).

[32] S. Lu, Q. Zhou, Y. Guo, Y. Zhang, Y. Wu, and J. Wang, Coupling a crystal graph multilayer descriptor to active learning for rapid discovery of 2D ferromagnetic semiconductors/half-metals/metals, Adv. Mater. **32**, 2002658 (2020).

[33] S.-S. Wang, Z.-M. Yu, Y. Liu, Y. Jiao, S. Guan, X.-L. Sheng, and S. A. Yang, Two-dimensional nodal-loop half-metal in monolayer MnN, Phys. Rev. Mater. **3**, 084201 (2019).

[34] Y. Feng, X. Wu, J. Han, and G. Gao, Robust half-metallicities and perfect spin transport properties in 2D transition metal dichlorides, J. Mater. Chem. C **6**, 4087 (2018).

[35] H. Xie, Y. Qie, I. Muhammad, and Q. Sun, 2D $CrCl_2(pyrazine)_2$ monolayer: High-temperature ferromagnetism and half-metallicity, J. Phys.: Condens. Matter **32**, 135801 (2019).

[36] Q. Sun, J. Li, Y. Li, Z. Yang, and R. Wu, Cr_2NX_2 MXene (X = O, F, OH): A 2D ferromagnetic half-metal, Appl. Phys. Lett. **119**, 062404 (2021).

[37] Q. Cui, Y. Zhu, Y. Ga, J. Liang, P. Li, D. Yu, P. Cui, and H. Yang, Anisotropic Dzyaloshinskii–Moriya interaction and topological magnetism in two-dimensional magnets protected by $P\bar{4}m2$ crystal symmetry, Nano Lett. **22**, 2334 (2022).

[38] See Supplemental Material at http://link.aps.org/supplemental/10.1103/PhysRevB.110.085130 for the discussion about the phonon dispersion and magnetic ordering of MX_2. The half-metallicty of MX_3 and predicted materials are also discussed. In addition, the half-metallicity with different functionals are compared.

[39] J. H. Jung, C.-H. Park, and J. Ihm, A rigorous method of calculating exfoliation energies from first principles, Nano Lett. **18**, 2759 (2018).

[40] Z. Guan and S. Ni, Prediction of high curie temperature, large magnetic crystal anisotropy, and carrier doping-induced half-metallicity in two-dimensional ferromagnetic FeX_3 (X = F, Cl, Br, and I) monolayers, J. Phys. Chem. C. **125**, 16700 (2021).

[41] H. Wang, V. Eyert, and U. Schwingenschlögl, Electronic structure and magnetic ordering of the semiconducting chromium trihalides $CrCl_3$, $CrBr_3$, and CrI_3, J. Phys.: Condens. Matter **23**, 116003 (2011).

[42] X. Cai, T. Song, N. P. Wilson, G. Clark, M. He, X. Zhang, T. Taniguchi, K. Watanabe, W. Yao, D. Xiao *et al.*, Atomically thin $CrCl_3$: An in-plane layered antiferromagnetic insulator, Nano Lett. **19**, 3993 (2019).

[43] L. Zhang, C. Tang, and A. Du, Two-dimensional vanadium tetrafluoride with antiferromagnetic ferroelasticity and bidirectional negative Poisson's ratio, J. Mater. Chem. C **9**, 95 (2021).

[44] H. Xiao, X. Wang, R. Wang, L. Xu, S. Liang, and C. Yang, Intrinsic magnetism and biaxial strain tuning in two-dimensional metal halides V_3X_8 (X = F, Cl, Br, I) from first principles and Monte Carlo simulation, Phys. Chem. Chem. Phys. **21**, 11731 (2019).

[45] H. Bai, Z. Yu, J. Feng, D. Liu, W. Li, and H. Pan, Co_3X_8 (X = Cl and Br): Multiple phases and magnetic properties of the kagome lattice, Nanoscale **16**, 1362 (2024).

[46] X. Bai, Y. Xue, K. Luo, K. Chen, Q. Huang, X.-H. Zha, and S. Du, Two-dimensional half-metallic and semiconducting lanthanide-based MXenes, ACS Omega **7**, 40929 (2022).

[47] G. Kresse and J. Furthmüller, Efficient iterative schemes for *ab initio* total-energy calculations using a plane-wave basis set, Phys. Rev. B **54**, 11169 (1996).

[48] G. Kresse and J. Furthmüller, Efficiency of ab-initio total energy calculations for metals and semiconductors using a plane-wave basis set, Comput. Mater. Sci. **6**, 15 (1996).

[49] P. E. Blochl, Projector augmented-wave method, Phys. Rev. B **50**, 17953 (1994).

[50] J. P. Perdew, K. Burke, and M. Ernzerhof, Generalized gradient approximation made simple, Phys. Rev. Lett. **77**, 3865 (1996).

[51] A. Togo and I. Tanaka, First principles phonon calculations in materials science, Scr. Mater. **108**, 1 (2015).

[52] J. Paier, M. Marsman, K. Hummer, G. Kresse, I. C. Gerber, and J. G. Ángyán, Screened hybrid density functionals applied to solids, J. Chem. Phys. **124**, 154709 (2006).

[53] X.-F. Liu, Z.-J. Luo, X. Zhou, J.-M. Wei, Y. Wang, X. Guo, B. Lv, and Z. Ding, Structural, mechanical, and electronic properties of 25 kinds of *III–V* binary monolayers: A computational study with first-principles calculation*, Chin. Phys. B **28**, 086105 (2019).

[54] L. Hammerschmidt, S. Schlecht, and B. Paulus, Electronic structure and the ground-state properties of cobalt antimonide Skutterudites: Revisited with different theoretical methods, Phys. Status Solidi A **210**, 131 (2013).

[55] H.-D. Saßnick and C. Cocchi, Electronic structure of cesium-based photocathode materials from density functional theory: Performance of PBE, SCAN, and HSE06 functionals, Electron. Struct. **3**, 027001 (2021).